Rotating Convective Disturbances in the Trades

David J. Raymond
Sharon A. Lewis
Physics Department and Geophysical Research Center
New Mexico Tech
Socorro, NM 87801

July 13, 1994

Summary

Observations of rotating convective disturbances in the Trade Wind region just east of Hawaii are presented. Rotation results from stretching of vertical ambient vorticity in the convective regions. Surface friction is shown to play a significant dissipative role in these disturbances. Ekman pumping associated with the rotation is probably only of secondary importance. Convection is found to be associated with weak local maxima in the boundary layer equivalent potential temperature. This suggests that convection occurs where such anomalies make the buoyancy of surface parcels larger than average. Convective available potential energies are found to be small, which means that such equivalent potential temperature anomalies are important in determining parcel buoyancy. We hypothesize that mesoscale circulations induced by the ascending motion of convection reinforce the anomalies, resulting in the intensification of the circulations. The equivalent potential temperature of the boundary layer results from a balance between surface fluxes and entrainment from above. Ascending motion apparently reduces entrainment, thus allowing the equivalent potential temperature to rise, whereas subsidence has the opposite effect.

1 Introduction

As seen from the window of an airliner, convection in the Trade Wind regions of the world seems to exhibit a great deal of organization on the $30-100$ km scale. This organization has not been much studied. The Hawaiian Rainband Project (HaRP), based on the windward side of the Island of Hawaii during July and August of 1990, therefore provided a unique opportunity to explore the dynamics of Trade Wind convective organization, at least to the extent that it survives upstream island effects.

The HaRP project provided us with two useful tools to study convection, namely the Electra aircraft of the National Center for Atmospheric Research (NCAR) and a pair of C-band Doppler radars from NCAR. The latter allowed us to characterize the morphology and kinematics of precipitating oceanic convection out to about 75 km, while the former made *in situ* thermodynamic and dynamic measurements out to about twice this distance. In addition, satellite imagery helped set the large scale scene.

In order to avoid confusing oceanic convective organization with that created by the island, we searched for convective disturbances that initially formed near or beyond the maximum range of the radars. Two disturbances during the HaRP project stood out in this regard. On 20 July a vortex similar to a tiny tropical storm occurred, while on 27 July a persistent rain-shower associated with a roughly north-south shear line moved onshore. The purpose of this paper is to document these two cases of oceanic convective organization and, if possible, to determine the governing dynamical processes.

The existence of strong vertical vorticity immediately brings to mind the possibility of Ekman pumping. This has long been considered a key mechanism for organizing oceanic convection (Charney and Eliassen, 1964; Ooyama, 1964; Charney, 1971). Whether Ekman pumping actually does so is a matter of dispute. If there is preexisting conditional instability, one may plausibly argue that the lifting produced by Ekman pumping can release this instability. However, in the absence of such instability, Ekman pumping won't produce more than very shallow clouds at the top of the boundary layer.

Independent of its effect on cumulus clouds, it is clear that Ekman pumping tends to spin down the vortex or shear line causing the pumping (Holton, 1972). This leads us to inquire about the energy source responsible for the spinup of these disturbances in the first place. Three possible sources of

energy are 1) ambient CAPE in the Trade Wind layer, 2) Energy release produced by the evaporation of precipitation, and 3) the thermodynamic disequilibrium between the sea surface and the atmosphere, as discussed by Emanuel (1986).

In order for moist convection to add available potential energy (APE) to an atmospheric disturbance, the convective heating must occur in a warm anomaly associated with the disturbance (Lorenz, 1955). Thus, the release of CAPE can only counter the destruction of APE at low levels by surface friction if the vortex is warm core (Emanuel, 1989).

The release of energy by evaporative cooling operates in the Rotunno-Klemp-Weisman (RKW) model of squall line propagation (Rotunno, Klemp, and Weisman, 1988), and is known to be central to the dynamics of many mesoscale convective systems. In contrast to heating, evaporative cooling increases APE when it takes place in a cold core vortex. Spinup in this case is aloft, just above the region of evaporative cooling, so it cannot oppose the frictionally induced spindown at low levels.

The ocean surface as an energy source is known to be central to the dynamics of hurricanes (Kleinschmidt, 1951; Riehl, 1954; Ooyama, 1969; Emanuel, 1986, 1988, 1989) and is suspected to to be of importance for the Madden-Julian oscillation (Madden and Julian, 1971, 1972, 1994; Emanuel, 1987, 1993; Neelin, Held, and Cook, 1987; Yano and Emanuel, 1991). Differential heating of the atmosphere associated with variations in the low level wind speed is the mechanism by which this energy source is postulated to create vertical circulations and the associated spinup of rotating disturbances. Such disturbances are necessarily warm in the region of enhanced convection, since otherwise the heating could not create APE.

The sea surface temperatures in the Trade Wind regions near Hawaii are significantly less than those in the equatorial western Pacific. However, the air temperatures are also less, and the degree of thermodynamic disequilibrium between the air and the ocean is almost as strong as that in the equatorial regions. It is therefore reasonable to expect to find disturbances driven by sea-air fluxes in the Trades. This paper shows that the disturbances we documented near Hawaii were most likely the ascending branches of mesoscale circulations driven by the sea-air fluxes of latent and sensible heat.

2 Theoretical considerations

In this section we first review the theoretical basis for vortex spinup in terms of vorticity dynamics. We then consider how surface heat and momentum fluxes can cause a mesoscale circulation to develop. In this paper *boundary layer* means that region below cloud base, while *marine* layer denotes everything below the Trade Wind inversion.

2.1 Absolute vorticity budget

The vorticity equation may be written

$$\frac{\partial \boldsymbol{\zeta}}{\partial t} + \nabla \cdot (\boldsymbol{v}\boldsymbol{\zeta} - \boldsymbol{\zeta}\boldsymbol{v}) + \nabla \times (\rho^{-1}\nabla p) - \nabla \times \boldsymbol{F} = 0, \tag{1}$$

where $\boldsymbol{v}$ is the velocity, $\boldsymbol{\zeta}$ is the absolute vorticity, ρ is the air density, p is the pressure, and $\boldsymbol{F}$ is the frictional force. The z-component of this equation may be written completely in flux form with horizontal fluxes only (Haynes and McIntyre, 1987, 1990):

$$\frac{\partial \zeta_z}{\partial t} + \nabla_h \cdot \left[\boldsymbol{u}\zeta_z + \boldsymbol{k} \times \left(\boldsymbol{F} - w\frac{\partial \boldsymbol{u}}{\partial z} \right) \right] = 0, \tag{2}$$

where $\boldsymbol{u}$ and w are the horizontal and vertical parts of $\boldsymbol{v}$, ∇_h is the horizontal gradient, ζ_z is the z-component of $\boldsymbol{\zeta}$, and $\boldsymbol{k}$ is a unit vector in the z-direction. The contribution of the vertical velocity to the horizontal components of the vorticity has been neglected, as has the slight vertical component of the baroclinic generation term.

The Ekman velocity, $\boldsymbol{u}_e$, is just that velocity which makes the vorticity flux term in (2) balance the force term:

$$\boldsymbol{u}_e \equiv -\boldsymbol{k} \times \boldsymbol{F}/\zeta_z. \tag{3}$$

This reduces to the usual form $|\boldsymbol{u}_e| = |\boldsymbol{F}|/f$ when the relative vorticity is small compared to the Coriolis parameter, f. Splitting the flow into Ekman and non-Ekman parts, $\boldsymbol{u} = \boldsymbol{u}_e + \boldsymbol{u}_n$, (2) becomes

$$\frac{\partial \zeta_z}{\partial t} + \nabla_h \cdot \left(\boldsymbol{u}_n\zeta_z - \boldsymbol{k} \times w\frac{\partial \boldsymbol{u}}{\partial z} \right) = 0. \tag{4}$$

Integrating over a horizontal area, A, the edges of which have $w = 0$, leads to

$$\frac{\partial}{\partial t}\int_A \zeta_z dA = \frac{\partial \Gamma}{\partial t} = -\oint_{\partial A} \zeta_z \boldsymbol{u}_n \cdot \boldsymbol{n} ds \tag{5}$$

where Γ is the absolute circulation around the periphery, ∂A, of A, $\boldsymbol{n}$ is the horizontal outward unit normal on ∂A, and the integral on the right side is a line integral on ∂A.

Integrating the anelastic mass continuity equation over A results in

$$\oint_{\partial A} \boldsymbol{u} \cdot \boldsymbol{n} ds = -\frac{1}{\rho}\frac{\partial}{\partial z}\int_A \rho w dA. \tag{6}$$

Combining this with (3) and (5) yields

$$\frac{1}{\overline{\zeta_z}}\frac{\partial \Gamma}{\partial t} = \frac{1}{\rho}\frac{\partial}{\partial z}\int_A \rho w dA - \oint_{\partial A} (\boldsymbol{k} \times \boldsymbol{F}/\zeta_z) \cdot \boldsymbol{n} ds, \tag{7}$$

where $\overline{\zeta_z}$ is the average of ζ_z on ∂A weighted by $\boldsymbol{u}_n \cdot \boldsymbol{n}$.

The total heating is the sum of the convective and radiative parts:

$$H(z) = H_c(z) + H_r(z). \tag{8}$$

Furthermore, the heating is closely related to the vertical velocity in the tropics by

$$H = w\frac{\partial \theta}{\partial z}. \tag{9}$$

This relationship arises from the fact that the temperature profile in the tropics doesn't change much with time, and in addition has weak horizontal gradients. Under these circumstances, heating can only be associated with vertical motion.

The vertical integral of the frictional force per unit volume, $\rho\boldsymbol{F}$, equals minus the surface stress. Representing the latter by a bulk formula with drag coefficient C_d, we can therefore write

$$\rho\boldsymbol{F} = -\rho_s C_d U^2 \boldsymbol{s}\sigma(z), \tag{10}$$

where $\sigma(z)$ represents the vertical distribution of the frictional force and $\boldsymbol{s}$ is a unit vector pointing in the direction of the boundary layer wind. The vertical integral of $\sigma(z)$ is unity. Solving (9) for w and combining with (10)

and (7) shows how the spinup of a disturbance can be related to physical processes in the atmosphere.

To make further progress we must establish what causes convection in the Trade Wind regions. When CAPE is non-zero, any mechanism that releases conditional instability, including Ekman pumping, can be said to cause convection. However, as (5) shows, if the inflow is precisely that associated with Ekman pumping, so that $\boldsymbol{u}_n = 0$, then neither spinup nor spindown occurs — the vortex is steady. If more convective mass flux occurs than can be accounted for by Ekman pumping, the disturbance spins up. This could happen, for instance, if unstable air just above the boundary layer were entrained into cumulus updrafts. On the other hand, if detrainment of rising air occurs near cloud base (see, *e. g.*, Raymond and Wilkening, 1980), then the net mass flux is less than implied by Ekman pumping, and the disturbance spins down. In the extreme case where there is no CAPE, Ekman pumping is ineffective in producing convection.

2.2 Diabatic heating and cooling

We now turn to the possibility that sea-air fluxes can drive convection in the Trade Wind regions. Sea surface temperatures near Hawaii are approximately 26° C, leading to a typical saturated sea surface equivalent potential temperature of $\theta_{ess} = 350$ K. [1] Boundary layer values of equivalent potential temperature are typically $\theta_{eb} = 335$ K, or about 15 K lower.

We characterize the total heat flux into the atmosphere from the sea surface by a bulk flux formula for the equivalent potential temperature (Gill, 1982):

$$F_e = C_e U(\theta_{ess} - \theta_{eb}), \tag{11}$$

where $C_e \approx 10^{-3}$ is a bulk transfer coefficient and U is the boundary layer wind speed. In a boundary layer of depth b in which surface fluxes are the only influence on the boundary layer equivalent potential temperature, θ_{eb} would obey

$$\frac{d\theta_{eb}}{dt} = U\frac{\partial\theta_{eb}}{\partial s} = \frac{C_e U \Delta\theta_e}{b}, \tag{12}$$

[1] The reversible equivalent potential temperature (Emanuel, 1994) is used exclusively in this paper. At low levels in the tropics this reads about 8 K lower than the pseudoadiabatic equivalent potential temperature.

where s is the displacement in the direction of the boundary layer wind and $\Delta\theta_e = \theta_{ess} - \theta_{eb}$ is the sea-air thermodynamic disequilibrium. We define the *specific recharge length* of the boundary layer as

$$\Lambda \equiv \left(\frac{\partial \theta_{eb}}{\partial s} \right)^{-1} = \frac{b}{C_e \Delta\theta_e}. \tag{13}$$

If $b = 600$ m, $C_e = 10^{-3}$, and $\Delta\theta_e = 15$ K, then $\Lambda = 40$ km K^{-1}. As we shall see, a 1 K increase in θ_{eb} is potentially significant to the generation of convection. Thus, sea-air entropy fluxes are likely to be important for disturbances on this scale.

If entrainment of air into the boundary layer from above is important, then (12) acquires an additional term:

$$\frac{d\theta_{eb}}{dt} = \frac{U}{\Lambda} - \frac{w_e \delta\theta_e}{b}, \tag{14}$$

where w_e is the entrainment velocity (the volume per unit surface area per unit time of cloud layer air incorporated into the boundary layer) and $\delta\theta_e$ is the jump in θ_e from the cloud layer to the boundary layer. In a steady state the two terms on the right side of this equation balance. The subsidence velocity required to maintain equilibrium with observed Trade Wind conditions is

$$w_e = \frac{Ub}{\Lambda \delta\theta_e} = \frac{C_e U \Delta\theta_e}{\delta\theta_e}. \tag{15}$$

Assuming typical Trade Wind conditions with $C_e = 10^{-3}$, $U = 7$ m s^{-1}, $\Delta\theta_e = 15$ K, and $\delta\theta_e = 5$ K, we find $w_e = 0.02$ m s^{-1}. This far exceeds the climatological average for the Trades of a few millimeters per second (see, *e. g.*, Betts and Ridgway, 1989). However, it is consistent with what would be found in mesoscale flows with horizontal scale of order 100 km and horizontal wind perturbations of a few meters per second.

A measure of the strength of convective heating produced by sea-air fluxes in the steady state can be made in the following way. To a good approximation, changes in θ, θ_e, and the water vapor mixing ratio, r, are related by

$$\frac{d\theta_e}{\theta_e} = \frac{d\theta}{\theta} + \frac{L\,dr}{c_p T_R}, \tag{16}$$

where L is the latent heat of condensation, c_p is the specific heat of air at constant pressure, and T_R is a reference temperature, say 300 K. Assuming that the surface flux of θ_e is ultimately distributed through the depth of the marine layer, d, then

$$\begin{aligned} \rho_s F_e &= \int_0^d \rho \left(\frac{\partial \theta_e}{\partial t} \right)_{fl} dz \\ &= \int_0^d \frac{\rho \theta_e}{\theta} \left(\frac{\partial \theta}{\partial t} \right)_{fl} dz + \frac{L}{c_p T_R} \int_0^d \rho \theta_e \left(\frac{\partial r}{\partial t} \right)_{fl} dz, \end{aligned} \tag{17}$$

where $\rho_s = \rho(0)$, and where the subscripted fl indicates the contribution to the rate of change of the variable in question from the surface heat flux. Thus, the total sea-air heat flux is divided between heating and moistening the convective layer.

Identifying $(\partial\theta/\partial t)_{fl}$ with the convective heating, H_c, and ignoring the effect of radiation so that $H = H_c = w(\partial\theta/\partial z)$, equation (17) can be written

$$\epsilon_p \rho_s F_e = \int_0^d \frac{\theta_e}{\theta} \frac{\partial \theta}{\partial z} (\rho w) dz, \tag{18}$$

where ϵ_p is the fractional contribution of the first term on the right side of (18) to the entire right side. Since convective heating is accompanied by precipitation, ϵ_p can also be characterized as a precipitation efficiency (Yano and Emanuel, 1991; Emanuel, 1993).

Integrating both sides of (18) over some horizontal area, A, yields

$$\epsilon_p \rho_s \int F_e dA \equiv \epsilon_p \rho_s \overline{F_e} A = \int \int_0^d \frac{\theta_e}{\theta} \frac{\partial \theta}{\partial z} (\rho w) dz dA, \tag{19}$$

where $\overline{F_e}$ is the areal mean of F_e. The area A may be interpreted as the areal extent of the surface fluxes required to feed the convection represented by the right side of (19).

3 The HaRP experiment

Figure 1 shows a map of the target area of the Hawaiian Rainband Experiment (HaRP). This program had many facets, but the tools of primary interest to us are the Doppler radars and the Electra aircraft, both provided

by the National Center for Atmospheric Research (NCAR). Times and dates are in UTC time unless otherwise noted. Local time in Hawaii is UTC - 10 h.

3.1 Radar data

The two Doppler radars used in HaRP were CP-3 and CP-4. CP-4 was located at the Hilo airport on the Island of Hawaii. Its location was taken as the origin of our Cartesian coordinate system, with x extending east from there and y extending north. CP-3 was 17.5 km southeast of CP-4 along the eastern coastline of the island.

Both radars operated at a wavelength of 5.5 cm. The individual radars had a maximum range of about 76.8 km. However, the optimum dual Doppler zone was located $10 - 30$ km offshore. This configuration was chosen to provide the best possible observations of island-induced rainbands, the primary focus of the project. However, our interest is in convective systems that developed well offshore and moved toward the island. Thus, we must frequently deal with systems that are not ideally situated for dual Doppler analysis.

The scan pattern followed by the two radars consisted of 5 successive coplane volume scans (Miller and Strauch, 1974) interspersed with other scanning modes. We make use of only the coplane volumes.

In a coplane scan the two radars sweep a common plane containing the two radars. This plane is referred to as a coplane. The angle made by the plane with the horizontal is called the coplane angle, α. A volume scan is acquired by successively incrementing α.

The coplane scanning method assumes that the velocity field is stationary only during the time necessary to scan one plane. This is an advantage over conventional scanning methods in which the velocity fields are assumed constant during the entire volume scan. The volume scan time for the HaRP study was about 2.5 minutes, with 12 planes per volume.

The traditional method for coplane analysis is to interpolate the data to cylindrical coordinates where it is analyzed. The data are then interpolated to Cartesian coordinates (Miller and Strauch 1974). Instead of using the traditional method, we interpolated the data directly to the Cartesian grid centered at CP-4. The grid spacing was taken to be 0.5 km in all directions.

The interpolation of radar ray data to the Cartesian grid was done by making a weighted average of all data points inside a box of two grid di-

mensions in each direction, with the analyzed point at the center of the box. Data points closer to the analysis point were given a greater weight in the averaging process.

An approximate correction was made for the curvature of the earth, so that the grid is not precisely Cartesian, but is "warped" to make grid elevations true elevations above sea level. This is a relatively minor effect for the ranges considered in this project.

Once the data were interpolated to a common grid, reflectivity plots were used to determine the storm velocity in each case study. Since the translation speeds of the observed storms reached 8 m s^{-1}, the storms moved up to 1.2 km during the time necessary to do a volume scan. Therefore, after the storm velocity was determined, the interpolation to Cartesian coordinates was redone with the position of each ray data point advected to a common time based on the measured translation speed. This time was chosen to be the start of the volume scan. The air velocity components were determined using a method described in the Appendix.

3.2 Electra aircraft data

The Electra carried standard thermodynamic, wind, and particle sensing instrumentation. We used the Rosemount temperature sensor and a cooled mirror dewpoint instrument to determine the temperature and humidity, and hence the equivalent potential temperature. The Rosemount thermometer is known to produce anomalously low temperatures in cloud or rain due to wetting of the temperature element in an airstream that has been warmed and desaturated by aircraft-motion-induced compression. Thus, the interpretation of Rosemount temperatures in these circumstances needs to be made with care. The behavior of the dewpoint instrument in cloud and rain is unknown.

Wind measurements are made by adding the aircraft-relative wind to the known velocity of the aircraft relative to the ground. The former velocity is determined by the Electra's radome gust probe and the latter by the aircraft's Litton Instruments inertial navigation system (INS). Global Positioning System (GPS) positions were available for some flights, but were not useful for either flight of interest in this paper. Therefore we used only information from the INS to determine the winds and aircraft position. Respective errors are of order 1 m s^{-1} and several kilometers.

The placement of the precipitation particle probes on the Electra during HaRP was not ideal. Apparently aircraft-induced shear and turbulence broke up large raindrops before they entered the probes, resulting in the detection of no drops larger than 3 mm in situations in which larger drops are known to exist. We only use these instruments for the qualitative determination of the presence or absence of cloud and rain.

4 Case studies

In this section we describe the two cases of interest. Both of these case studies were made in disturbed Trade Wind conditions. The base of the Trade Wind inversion ranged as high as 650 mb in these cases, which is somewhat higher than the average value.

4.1 20 July 1990

A deep but weak Trade Wind flow existed at the start of operations on 20 July 1990. At 1518 h (0518 LST) the environmental flow offshore was found to be from the southeast, and there was a broad, but weak east-west band of precipitation east of CP-4. The Electra launched at 1458 h and the radars began coplane scans at 1539 h. At 1754 h a cyclonic rotation was noticed in a large, amorphous mass of cloud $10 - 40$ km east-northeast of CP-4. The Electra was sent into this disturbance. However, at 1852 h another, stronger vortex was noted in the real time Doppler radar display bearing 100° at 60 km from CP-4. The Electra was then vectored toward this vortex, and the coplane scans of the radars were optimized to study this system. The Electra made roughly north-south passes through the vortex from 1910 h to 2048 h, after which it returned to base. The vortex moved toward the west at about 3.3 m s^{-1} during the period of observation, and coplane scans were continued until about 2100 h.

Figures 2 and 3 show storm-relative winds (*i. e.*, with the 3.3 m s^{-1} westward movement subtracted) and the reflectivity in the vicinity of the vortex at 1926 h and 2017 h and $z = 1$ km. Note that the vortex has a radar "eye" about 5 km in diameter, and that the highest reflectivities are on the north side of the eye. The eye is better developed at the later time. However, note that the areal extent of reflectivity exceeding 20 dBZ decreased between

the two times. The storm-relative winds show a nearly symmetric circulation about the center of the vortex. However, in earth-relative coordinates the strongest winds are on the north side of the eye where the highest reflectivities are found.

The Electra made a sounding in clear air 140 to 180 km east-northeast of CP-4 from 1513 h to 1518 h. At this time the vortex would have been 80 km east of CP-4, which means that the sounding was taken approximately 100 km northeast of the vortex.

The sounding is presented in figure 4 in slightly unconventional form (Betts, 1974), which requires a few words of explanation. The equivalent potential temperature, θ_e, and the saturated equivalent potential temperature, θ_{es}, are plotted against pressure in figure 4. In addition, contours of constant potential temperature, θ, are shown as dashed lines. Recalling that θ and θ_e are conserved in dry motions, the changes in the values of θ_e and θ_{es} in the ascent of a surface parcel are described by the vertical and slanted lines in figure 4. Saturation is reached where these two lines meet. In subsequent ascent $\theta_e = \theta_{es}$, and both follow the vertical line.

For both the saturated and unsaturated phases of the ascent the parcel buoyancy is proportional to the difference between the parcel and environmental θ_{es} curves. Thus, a surface parcel is nearly neutral in ascent to about 975 mb, with negative buoyancy until 920 mb. Further ascent yields positive buoyancy until about 660 mb, with the exception of a small region of negative buoyancy near 740 mb.

The wind at the surface was easterly at 7 m s^{-1}, with westerly shear, leading to a transition to westerly winds above 780 mb.

Figure 5 shows a thermodynamic sounding taken within about 15 km of the center of the vortex between 1937 h and 2000 h. As the right panel of figure 5 shows, the sounding occurred in a region of cloud. However, liquid water contents measured by the Forward Scattering Spectrometer Probe (FSSP) were quite small, rarely exceeding 0.15 g m^{-3}. Thus, the effect of wetting on the instruments should be minor in this ascent, and the profiles of θ_e and θ_{es} should be approximately correct.

The major conclusion from this sounding is that essentially no dry boundary layer existed in this region — the air was saturated down to about 1000 mb, and no potential energy barrier blocked the ascent of moist surface parcels. In addition, the low level equivalent potential temperature was about 1 K higher than the value in the sounding shown in figure 4 — 336 K

rather than 335 K. In spite of this increase, parcel buoyancy near 800 mb was actually less than in the clear air sounding.

The lack of a dry boundary layer was confirmed by visual observations of the Electra flight scientist. No distinct cloud base existed and ragged strands of cloud extended down to the surface within the vortex.

The storm-relative westerly wind component at 2017 h is shown in the vertical, north-south cut of figure 6. This cut is taken through the center of the vortex, and linear interpolation of the velocity followed by smoothing was done to give an estimate of how the velocity varies across the echo-free region of the vortex eye. The center of the vortex is at roughly $y = -7$ km. Maximum storm-relative easterlies of 4 m s^{-1} occur north of the center at $y = 0$ km, while maximum westerlies of 5 m s^{-1} occur south of the center at $y = -11$ km. Thus, the average tangential velocity around the vortex is about 5 m s^{-1} and the radius of maximum wind is about 5.5 km.

Near the vortex the tangential winds decrease with height above $1 - 1.5$ km. The vortex core tilts slightly to the north and the vortex signature is still weakly visible at the radar-observed cloud top of $3.5 - 4$ km.

Figures 7 and 8 show the horizontal divergence, $\nabla_h \cdot \boldsymbol{u}$, and absolute vorticity, ζ_z, at the time and elevation of figure 3. To obtain these fields, the velocity field is linearly interpolated in x and y through missing data regions. The divergence and vorticity are then calculated using centered differences and the results are smoothed in x and y using a low pass filter with a 3 km cutoff. The purpose of this procedure is to obtain estimates of the vorticity and divergence in regions of missing data (*e. g.*, the eye) that are surrounded or nearly surrounded by good data. Its effect is to assign constant values of divergence and vorticity to bad data regions that are consistent via the theorems of Gauss and Stokes with the observed velocity values on the boundaries of these regions. When bad data are not completely surrounded by good data, these theorems are not strictly applicable. However, the interpolation procedure still yields reasonable results if the gap in the good data on the periphery of the bad data region is not too large.

The estimates of divergence and vorticity in the eye region are probably adequate. However, spurious values of divergence exist north of the line defined by $x/90 + y/30 = 1$ as the interpolation here is over data voids that are not well surrounded by good data. These regions are therefore masked out in figures 7 and 8.

Several conclusions may be drawn from figures 7 and 8. First, as expected,

the largest vorticities are concentrated in the vicinity of the vortex — values as high as 1.6 ks^{-1} are seen there. This region of peak vorticity seems to be a part of a band of enhanced vorticity that stretches east-northeast to west-southwest. Interestingly enough, a band of convergence is colocated with the band of enhanced vorticity. At earlier times this region had reflectivities everywhere exceeding 20 dBZ. At the analysis time the region of strongest reflectivity is located generally on the band of convergence, but in regions where the convergence is a minimum, suggesting that convergence is somewhat suppressed there by the evaporation of rain.

This correlation between reflectivity and convergence suggests that the convergence is not an artifact of the analysis even though it occurs mostly beyond the region of optimal dual Doppler synthesis. A final point of interest is that the vorticity generally exceeds the divergence by a factor of 2 or more over the region of the major band. Thus, on the scales passed by the low pass filter, the Froude number is less than unity and the disturbance may be describable in terms of nearly balanced dynamics using a nonlinear balance model (Raymond, 1992).

The storm-relative inflow to the high reflectivity region north of the vortex is from the east. Figure 9 shows the flow in a vertical, east-west plane averaged over $0 \leq y \leq 5$ km. The domain for this figure is shown by the narrow rectangle in figure 3. The averaging removes much of the error generated by the unfavorable dual Doppler geometry for this case. The updraft takes the form of a rather gradual upglide toward the west, with weak downward motion below 2 km in the region of highest reflectivity. The updraft itself is broad and weak, with w everywhere less than 3 m s^{-1}. The weakness of the updraft is qualitatively consistent with the small CAPE implied by the in-storm sounding shown in figure 5.

Figures 10 and 11 show two north-south passes by the Electra through the vortex, the first centered at 1928 h at an elevation of 200 m, the second at 2016 h at an elevation of 650 m. At the earlier time the Electra navigation erroneously located the vortex center about 5 km south of its radar-derived location. This error is much less at the second time.

At the earlier time only very light precipitation was detected by the PMS 2D-C probe. At the later time somewhat higher precipitation rates were found at the north and south edges of the vortex eye. Of particular interest is the maximum in equivalent potential temperature that is seen near the center of the eye on the earlier pass and on the south edge on the later pass.

At 200 m the maximum is near 337 K. North of the vortex (presumably in the middle of the high reflectivity area there) the measured equivalent potential temperature drops to 335 K and returns to near $336-337$ K at the northern limit of the aircraft traverse. South of the vortex values near 333 K are found.

4.2 27 July 1990

On 27 July 1990 a variety of rainbands were studied using the radars and the Electra aircraft. However, the easternmost band stood out in comparison to the others, in that it was deeper and was associated with a nearly north-south line of convergence and shear. This is the storm on which we concentrate.

Unlike the 20 July case, the storm was observed in its intensifying stage. It also was embedded in relatively strong Trades, so that it advected to the west-southwest at a much higher speed than the 20 July storm, *i. e.* at about $(-8, -3)$ m s^{-1}.

Figures 12 - 14 show the storm at 0532 h, 0609 h, and 0632 h. The rapid growth in storm area with time is evident from these figures. Maximum reflectivities for this system exceeded 40 dBZ, compared with 25 dBZ for the 20 July case. It is also clear that the storm was coincident with a nearly north-south wind discontinuity. Relative to the above-quoted storm velocity, the wind was westerly on the west side of the storm and southerly on the east side. The discontinuity is therefore both a line of convergence and cyclonic shear.

Figure 15 shows an east-west vertical section of storm-relative winds at 0632 h. The section is averaged in the north-south direction over the most active segment of the convection. The averaging area is shown as the middle rectangle in figure 14. Notice that low level inflow comes from both sides of the convective line, but is stronger from the west side. The updraft tilts to the east, and is west of the zone of horizontal shear, which itself tilts to the east with height. The strongest southerly winds are not at the surface, but are east of the shear line near $z = 1$ km.

For purposes of comparison with the 20 July case, the divergence and vorticity at $z = 0.5$ km are shown in figures 16 and 17. These patterns were obtained by filling as many holes as possible with linear interpolation in x and y, smoothing the fields with a 2 km low pass filter, and then masking out the regions that had reflectivity less than 10 dBZ. This reduces noise on

the boundaries of the good data regions. Unlike the 20 July case there are no important holes in the reflectivity pattern that would have been lost by the masking procedure. The convergence is somewhat stronger than for the 20 July case, and no divergence is evident in the radar-observable area.

The absolute vorticity field shows vorticity perturbations that are similar in size and intensity to those in the 20 July case. In particular, the strong vorticity near $(35, 5)$ km is comparable to that in the vortex of 20 July. However, no radar eye had developed in the 27 July system up to the time it moved onshore.

The Electra aircraft made several soundings during its flight on 27 July. The sounding from 0311 h to 0327 h shown in figure 18 fortuitously occurred near the extrapolated position of the shear line and associated storm at that time. Evidence that the Electra actually crossed the shear line during the sounding comes from the sharp wind changes between 750 and 800 mb. The part of the sounding below this level probably took place west of the shear line.

The sounding is distinguished by its negligible values of parcel buoyancy. Recall that the low level segment of this sounding was taken on the west side of the storm, which from figure 15 is the inflow side. The wind profile shows a shallow region of strong westerly shear near the surface with a nearly constant westerly component from the top of the shear layer to near 800 mb. Nearly constant southerly shear is seen from the surface to 800 mb. The Trade inversion is between 650 and 700 mb in this sounding and the lifting condensation level (LCL) is roughly 990 mb, or only about 200 m above the surface. Surface air has $\theta_e = 339$ K and $\theta_{es} = 343$ K.

A second Electra sounding is shown in figure 19. This sounding was taken from 0155 h to 0205 h about 150 km southwest of the storm, and has a strikingly different character from the previously discussed sounding. First of all, the sounding is unconditionally stable and somewhat dryer. The Trade inversion is between 750 and 800 mb, or 100 mb lower than in the previous case. The easterly winds below 800 mb are much weaker than in figure 18. The sounding was taken $80 - 100$ km offshore, so there is unlikely to be any serious island influence. The boundary layer $\theta_e = 337$ K, or 2 K less than the value near the shear line, while $\theta_{es} = 344$ K, or 1 K more. The LCL for surface air is 970 mb, or near 400 m, which is twice the previous value.

A number of traverses were made by the Electra near $z = 200$ m. The winds, θ_e, and θ_{es} for these traverses are shown in figure 20 mapped to a

coordinate system moving with the storm. This figure confirms the picture of higher θ_e and lower θ_{es} near the storm and shows anticyclonic turning of the wind southwest of the storm.

A single later traverse crossing the shear line was made near $z = 300$ m (the onset of darkness necessitated the increase in altitude), and is shown in figure 21. The sharp cyclonic shear and the convergence (assuming a roughly north-south line orientation) are evident in this traverse. Also clear is the decrease in the difference between θ_{es} and θ_e near the storm.

5 Discussion of mechanisms

It is clear from the analysis of section 2 that the latent heating from convection must play a significant role in spinning up cyclonic disturbances in the Trades. Ekman pumping, though possibly instrumental in lifting air to the level of free convection, actually tends to spin down the cyclonic disturbance responsible for the pumping in the first place.

It is possible to estimate the balance between frictional dissipation and intensification by convective heating with the data at hand. Figure 22 schematically represents the 27 July case, with the shaded areas showing convective cells along the shear line, indicated by the thick dashed line. The line integral in (7) may be integrated around the box ABCD shown in this figure. In the case where the system is slab-symmetric, the contributions from the segments BC and DA cancel each other, leaving only the AB and CD segments. In these segments only the y-component of $\boldsymbol{F}$, F_y is important. We assume $\sigma(z) = 1/b$ for $z < b$ and zero above that level. For b of order the boundary layer depth, $\rho(z) \approx \rho_s$ and $F_y \approx -C_d U U_y / b$ from (10), where U_y is the y-component of the boundary layer wind, U. The line integral in (7) therefore becomes

$$L = \oint_{\partial A} (\boldsymbol{k} \times \boldsymbol{F}/\zeta_z) \cdot \boldsymbol{n} ds \approx \frac{C_d \Delta(U U_y) Y}{\zeta_0 b} \tag{20}$$

where ζ_0 is the ambient absolute vorticity away from the storm, $\Delta(UU_y)$ is the difference in UU_y between the AB and CD segments of the line integral, and Y is the length of the AB and CD sides of the box.

Assuming that all significant vertical motion is radar-visible, the first

term on the right side of (7) which is the areally integrated convergence,

$$K \equiv \frac{1}{\rho}\frac{\partial}{\partial z}\int_A \rho w dA \tag{21}$$

may be computed directly from radar observations. The right side of (7), $K - L$, may therefore be estimated.

Figure 23 shows a vertical profile for K computed over the part of the 0632 h volume of 27 July shown by the large rectangle in figure 14. The average value of K over the lowest 500 m is about 75 km^2 ks^{-1}. From figure 21, $UU_y \approx 0$ on the left side of the line because $U_y \approx 0$ there. On the right side of the line the x-component of U, $U_x \approx -8$ m s^{-1} in the reference frame of the earth, while $U_y \approx 5$ m s^{-1}. Thus, $\Delta(UU_y) \approx 50$ km^2 ks^{-2}. If $C_d \approx 10^{-3}$, $b \approx 0.5$ km, $Y \approx 20$ km, and $\zeta_0 \approx f \approx 0.05$ ks^{-1}, then $L \approx 40$ km^2 ks^{-1}, and K is about twice L, resulting in a tendency to spin up.

A rather different situation exists for the 20 July case. Figure 24 shows the integrated convergence profile, K, for 2017 h. In this system the convergence is distributed over a much greater depth, and the value of K at the surface is only about 25 km^2 ks^{-1}. The value of L is harder to calculate due to the lack of slab symmetry, but a rough estimate yields $L \approx 90$ km^2 ks^{-1}. Thus, $L > K$ in this case and the disturbance should have been spinning down.

The main sources of error in these estimates are in the frictional term, L. However, even if the bulk parameterization for friction is off by up to 50%, the same qualitative conclusions are reached. In both cases these conclusions agree with the observed behaviors of the respective systems. The radar-visible area of the 27 July storm was rapidly expanding with time, while the 20 July storm appeared to be dissipating.

The reflectivity values and the vertical profile of convergence for the 20 July case suggest a largely stratiform system, while the 27 July case consists of vigorously growing convection with little stratiform component. If Trade Wind systems undergo the same type of evolution that is seen in deep tropical convection (see, *e. g.*, Houze, 1981), then the 27 July storm was observed early in its life cycle whereas the 20 July storm was in a late phase. The deep region of inflow in the latter contrasts with the shallow inflow in the former, in agreement with this scenario.

One aspect in which the observed Trade Wind disturbances differ from deep tropical convection is in the absence of downward transport of air with very low values of equivalent potential temperature. This is probably because

such low θ_e air simply doesn't exist in the marine layer where it would be accessible to evaporative cooling by precipitation. Though such air exists above the Trade Wind inversion and is known to be entrained into the marine layer, the clouds seem to be unable to transport this air to the surface without substantial dilution by marine layer air.

In both cases reported here the CAPE available to convection in the convectively active regions was minimal. Thus, convection must have been tightly coupled to sea-air fluxes of energy in these disturbances. Given the estimated specific recharge length for equivalent potential temperature of 40 km K^{-1}, a traversal of 100 km of ocean would be sufficient for a boundary layer air parcel to acquire the typical 2 K excess of θ_e observed in convectively active regions compared to quiescent regions. This, of course, assumes that boundary layer air is not strongly diluted by subsiding marine layer air with lower values of equivalent potential temperature. However, the abnormally low lifting condensation levels seen in these systems means that the subcloud layer would recharge even more rapidly than estimated above. In addition, as we now discuss, the incorporation of *some* lower equivalent potential temperature air from above is crucial in setting up an instability that may ultimately be responsible for the 100 km structure of disturbances in the Trades.

Imagine the following instability mechanism. Assume that the equilibrium boundary layer equivalent potential temperature results from the balance described in (14) between surface fluxes, which tend to increase its value, and entrainment of air from above, which tends to decrease it. If a region somehow acquires a slight excess of θ_e in the marine layer, the entrainment of marine layer air into the boundary layer will not reduce θ_e there as much, resulting in a tendency toward higher boundary layer equivalent potential temperature. This in turn will result in increased boundary layer parcel buoyancy and a tendency for upward motion.

The upward motion will result in inflow at low levels and outflow at upper levels, with subsidence surrounding the region of ascent. Subsidence will increase $\delta\theta_e$, amplifying the effects of entrainment there. The opposite will happen in the ascending region. As a result, the boundary layer θ_e will further decrease in subsidence regions and increase in regions of ascent. Note that this mechanism depends on there being no low equivalent potential temperature downdrafts in convective regions.

The boundary layer air in the subsidence region will ultimately flow back

into the ascending region. Since this air acquires a low value of θ_e in the subsidence region, it must have a chance to increase its θ_e enroute to the convective area — otherwise convection there will be short-lived and the incipient disturbance will collapse. This recharge could happen in a number of ways — as (14) shows, the vertical gradient of θ_e and the subsidence velocity could decrease in the recharge region, and the surface wind speed could increase there. Figure 25 shows a schematic illustration of this instability mechanism.

Since this mesoscale circulation is taking place in a region of nonzero absolute vorticity, it naturally results in the spinup of the ascent region and the spindown of the subsidence region at low levels. However, surface friction is primarily dissipative in this scenario, since convection is assumed to be caused by increased low level parcel buoyancy rather than by convergence. Ekman pumping plays at most a secondary role in organizing the convective pattern, since the CAPE is small.

As a final check on the notion that the observed convective systems are being fed by a mesoscale instability that extracts energy from the sea surface, we use (19) to estimate the sea surface area required to feed the convection on 27 July located inside the large rectangle in figure 14. If $C_e = 10^{-3}$, $U = 8$ m s^{-1}, and $\Delta\theta_e = 15$ K, then $F_e = 0.12$ K m s^{-1}, which corresponds to a total surface heat flux of about 160 W m^{-2}. Using w from Doppler radar measurements and assuming $\epsilon_p = 1$, we find $A \approx 7000$ km^2, which corresponds to a square about 80 km on a side. This is commensurate with the apparent dimensions of the mesoscale circulation hypothesized in figure 25. Similar results are obtained for the 20 July case.

Fiedler (1993) presented the results of a three-dimensional simulation of dry convection with poorly conducting boundaries. Convective cells with very large aspect ratios were found in these calculations. We speculate that the observed disturbances share dynamical characteristics with this simulation. In both cases extended proximity to the surface is required for parcels to acquire enough energy to convect. This may explain the large aspect ratios seen in the convective cells in both cases.

6 Conclusions

These two case studies provide ample evidence for dynamic and thermodynamic structure on the $30-100$ km scale in the Trade Wind regions. Factors that significantly vary on this scale are the wind field, the potential temperature and equivalent potential temperature of the boundary layer, the lifting condensation level, and the height of the Trade Wind inversion. Rotating convective systems are coupled to the mesoscale structure in these two cases.

We hypothesize that the observed mesoscale circulations result from an instability that tends to reinforce mesoscale equivalent potential temperature anomalies. The key assumption is that regions of anomalously high boundary layer equivalent potential temperature exhibit higher than average parcel buoyancies, and hence mean ascending motion. The correlation between higher θ_e at low levels and convection holds in both of the case studies. Furthermore, observed values of CAPE are nearly always very small, which means that the buoyancy enhancement due to increased low level θ_e is important in these systems.

The rotation present in the two observed cases undoubtably resulted from simple stretching of absolute vorticity by the upward motion associated with the convection. We suspect that Ekman pumping played at most an incidental role in forcing these systems, since there is little or no ambient CAPE for this mechanism to release — the vertical motion is most likely free convective in origin, and is controlled by boundary layer thermodynamics. Surface friction plays an important dissipative role.

These studies documented situations that are probably not typical of ambient Trade conditions – cloud bases were lower than the nominal $500-600$ m and the top of the marine layer was higher than the usual 850 mb. However, since two similar cases occurred only a week apart, it seems unlikely that this type of situation is rare. Though we have not made a systematic survey of events during the full period (six weeks) of the HaRP project, a few other similar, but perhaps weaker, situations may have developed during that period.

Aside from scale, the main way in which the observed systems differ from deep tropical convection appears to be in the lack of low equivalent potential temperature downdrafts. Recent work by Emanuel (1989) suggests that this difference is crucial in the behavior of convection over warm water — it is much easier to spin up low level vortices when downdrafts are weak or absent.

The present results certainly support this contention. They also suggest that downward entrainment of low θ_e air into the boundary layer is as important a control on boundary layer equivalent potential temperature as surface fluxes and deep convective downdrafts.

Unlike Emanuel's (1989) finite amplitude tropical cyclogenesis mechanism, the instability postulated here is linear, implying that the resulting convective systems should be quite common in disturbed Trade Wind conditions. Existing evidence is sketchy, but does not rule out this hypothesis.

Acknowledgments. The HaRP project involved the combined efforts of many people. We particularly wish to thank Al Cooper and Rit Carbone for their leadership in this program and Tom Schroeder for providing helpful information on satellite imagery. Mike Fullerton of the University of Hawaii at Hilo played an essential role in making local arrangements. Marcia Baker and Al Cooper were respectively the flight scientists on the Electra on 20 and 27 July. Michael Bannister helped out in the field phase of the HaRP project. The project would not have been possible without the dedication of NCAR's Atmospheric Technology Division. Their operation of both the Electra aircraft and the two radars was exemplary. We also acknowledge the support of the Scientific Computing Division at NCAR for their help in providing the radar data. David Johnson kindly provided a map of the Island of Hawaii in Postscript form. This work was supported by the Atmospheric Sciences Section of the National Science Foundation under Grant Nos. ATM-8914116 and ATM-9311735. Sharon Lewis acknowledges support from the New Mexico Tech Graduate Office from funds provided by the State of New Mexico.

Appendix

Doppler radar measures the projection of precipitation particle velocity along the radar beam:

$$V_i = \boldsymbol{v}_p \cdot \boldsymbol{r}_i = v_{px} r_{ix} + v_{py} r_{iy} + v_{pz} r_{iz}, \tag{22}$$

where V_i is the velocity measured by radar i, $\boldsymbol{v}_p$ is the particle velocity, and $\boldsymbol{r}_i$ is the unit vector from radar i to the point measured.

We first eliminate particle velocity in favor of air velocity, $\boldsymbol{v}_a$, in (22). The horizontal components of air and particle velocities are the same. The

vertical component of air velocity is:

$$v_{az} = v_{pz} - w_t, \tag{23}$$

where w_t is the terminal fall velocity of the particle. This is taken from Joss and Waldvogel (1970) to be

$$w_t = -2.6Z^{0.107} \text{ m s}^{-1}, \tag{24}$$

where Z is the radar reflectivity. Assuming two radars, we now solve (22) for the horizontal components, v_{ax} and v_{ay}, of the air velocity:

$$v_{ax} = \frac{r_{2y}V_1 - r_{1y}V_2}{(r_{1x}r_{2y} - r_{2x}r_{1y})} - (v_{az} + w_t)\frac{(r_{1z}r_{2y} - r_{2z}r_{1y})}{(r_{1x}r_{2y} - r_{2x}r_{1y})} \tag{25}$$

$$v_{ay} = \frac{r_{1x}V_2 - r_{2x}V_1}{(r_{1x}r_{2y} - r_{2x}r_{1y})} - (v_{az} + w_t)\frac{(r_{1x}r_{2z} - r_{2x}r_{1z})}{(r_{1x}r_{2y} - r_{2x}r_{1y})}. \tag{26}$$

Substituting (25) and (26) into the anelastic continuity equation,

$$\frac{\partial(\rho v_{ax})}{\partial x} + \frac{\partial(\rho v_{ay})}{\partial y} + \frac{\partial(\rho v_{az})}{\partial z} = 0, \tag{27}$$

leaves us with a partial differential equation in v_{az}, which is readily integrated upward from the surface where $v_{az} = 0$.

References

Betts, A. K., 1974: Thermodynamic classification of tropical convective soundings. *Mon. Wea. Rev.*, **102**, 760-764.

Betts, A. K., and W. Ridgway, 1989: Climatic equilibrium of the atmospheric convective boundary layer over a tropical ocean. *J. Atmos. Sci.,* **46,** 2621-2641.

Charney, J., 1971: Tropical cyclogenesis and the formation of the intertropical convergence zone. *Lectures in Applied Mathematics*, **13**, American Mathematical Society, 355-368.

Charney, J. G. and A. Eliassen, 1964: On the growth of the hurricane depression. *J. Atmos. Sci.,* **21,** 68-75.

Emanuel, K. A., 1986: An air-sea interaction theory for tropical cyclones. Part I: Steady state maintenance. *J. Atmos. Sci.,* **43,** 585-604.

Emanuel, K. A., 1987: An air-sea interaction model of intraseasonal oscillations in the tropics. *J. Atmos. Sci.,* **44,** 2324-2340.

Emanuel, K. A., 1988: The maximum intensity of hurricanes. *J. Atmos. Sci.,* **45,** 1143-1155.

Emanuel, K. A., 1989: The finite-amplitude nature of tropical cyclogenesis. *J. Atmos. Sci.,* **46,** 3431-3456.

Emanuel, K., 1993: The effect of convective response time on WISHE modes. *J. Atmos. Sci.,* **50,** 1763-1775.

Emanuel, K. A., 1994: Atmospheric convection. *Oxford*, 580 pp.

Fiedler, B. H., 1993: Cell broadening in three-dimensional thermal convection between poorly conducting boundaries. *Beitr. Phys. Atmosph.*, **66**, 173-181.

Gill, A. E., 1982: Atmosphere-ocean dynamics. *Academic Press*, 662 pp.

Haynes, P. H., and M. E. McIntyre, 1987: On the evolution of vorticity and potential vorticity in the presence of diabatic heating and frictional or other forces. *J. Atmos. Sci.,* **44,** 828-841.

Haynes, P. H., and M. E. McIntyre, 1990: On the conservation and impermeability theorems for potential vorticity. *J. Atmos. Sci.,* **47,** 2021-2031.

Holton, J. R., 1972: An introduction to dynamic meteorology. *Academic Press*, 319 pp.

Houze, R. A., 1981: Structures of atmospheric precipitation systems: A global survey. *Radio Science*, **16**, 671-689.

Joss, J., and A. Waldvogel, 1970: Raindrop size distributions and Doppler velocities. *14th Conf. on Radar. Meteor.*, American Meteorological Society, Boston.

Kleinschmidt, E., 1951: Grundlagen einer theorie der tropischen zyklonen. *Arch. Meteor. Geophys. Bioklim.*, **4a**, 53-72.

Lorenz, E. N., 1955: Available potential energy and the maintenance of the general circulation. *Tellus,* **7,** 157-167.

Madden, R., and P. R. Julian, 1971: Detection of a 40-50 day oscillation in the zonal wind in the tropical Pacific. *J. Atmos. Sci.,* **28,** 702-708.

Madden, R., and P. R. Julian, 1972: Description of global-scale circulation cells in the tropics with a 40-50 day period. *J. Atmos. Sci.,* **29,** 1109-1123.

Madden, R. A., and P. R. Julian, 1994: Observations of the 40-50 day tropical oscillation — a review. *Mon. Wea. Rev.*, **122**, 814-837.

Miller, L. J., and R. G. Strauch, 1974: A dual Doppler radar method for the determination of wind velocities within precipitating weather systems. *Rem. Sens. Env.*, **3**, 219-235.

Neelin, J. D., I. M. Held, and K. H. Cook, 1987: Evaporation-wind feedback and low-frequency variability in the tropical atmosphere. *J. Atmos. Sci.,* **44,** 2341-2348.

Ooyama, K., 1969: Numerical simulation of the life cycle of tropical cyclones. *J. Atmos. Sci.,* **26,** 3-40.

Ooyama, K., 1971: A theory on parameterization of cumulus convection. *J. Meteor. Soc. Japan,* **49,** (special issue), 744-756.

Raymond, D. J., 1992: Nonlinear balance and potential-vorticity thinking at large Rossby number. *Quart. J. Roy. Meteor. Soc.,* **118,** 987-1015.

Raymond, D. J., and M. Wilkening, 1980: Mountain-induced convection under fair weather conditions. *J. Atmos. Sci.,* **37,** 2693-2706.

Riehl, H., 1954: Tropical meteorology. *McGraw-Hill*, 392 pp.

Rotunno, R., J. B. Klemp, and M. L. Weisman, 1988: A theory for strong, long-lived squall lines. *J. Atmos. Sci.,* **45,** 463-485.

Yano, J.-I., and K. Emanuel, 1991: An improved model of the equatorial troposphere and its coupling with the stratosphere. *J. Atmos. Sci.*, **48,** 377-389.

Figures

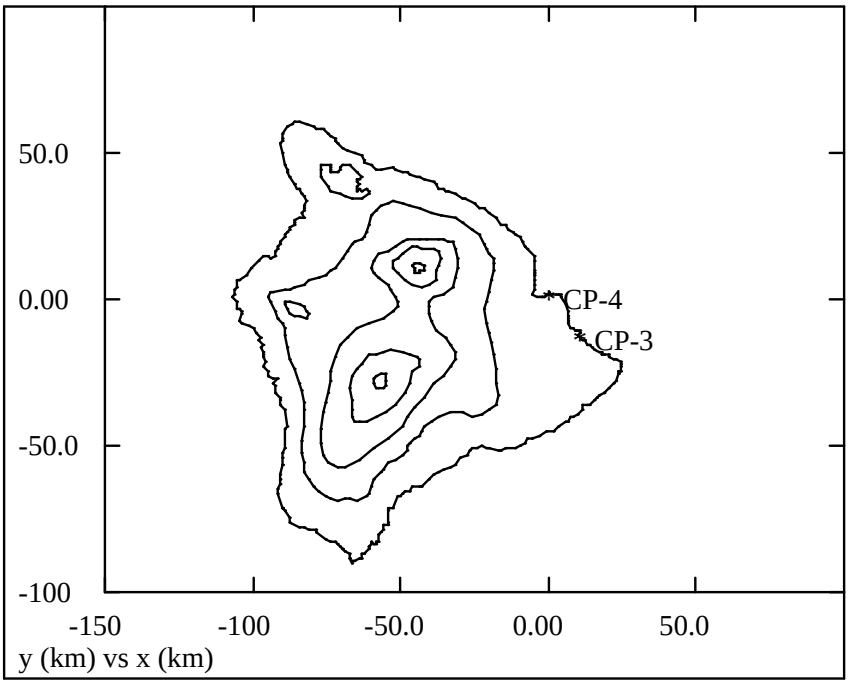

Figure 1: Map of the Island of Hawaii with the locations of the two radars marked. The elevation contours on the island are at intervals of 1 km. The coordinate system is centered at the radar CP-4.

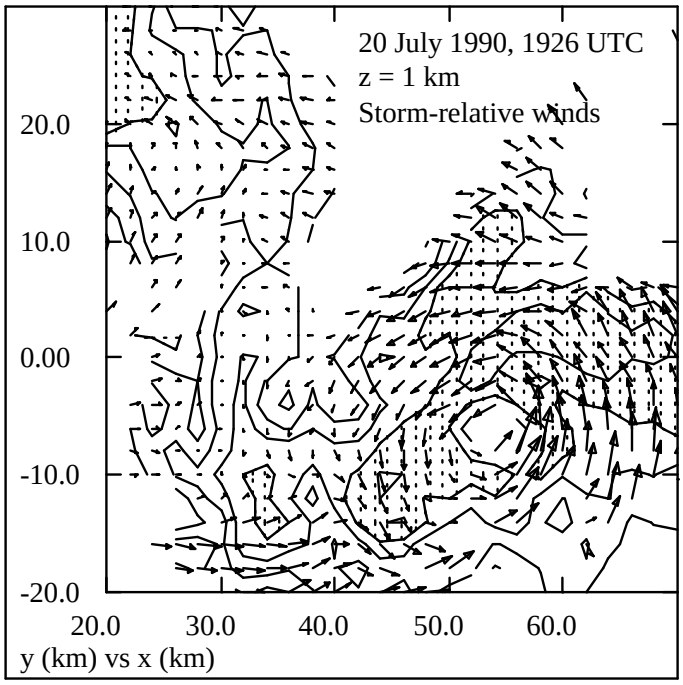

Figure 2: Storm-relative horizontal winds and reflectivity of vortex on 20 July 1990 at 1926 h and $z = 1$ km. The contour interval on reflectivity is 5 dBZ with reflectivities exceeding 20 dBZ hatched. The scale for wind vectors is 2.5 m s^{-1} km^{-1}. Data have been thinned to 2 km resolution for clarity.

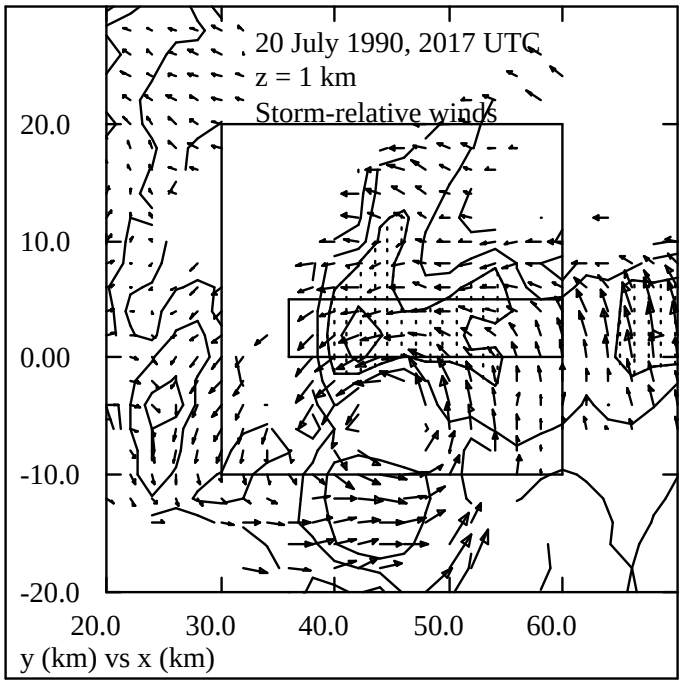

Figure 3: Storm-relative horizontal winds and reflectivity of vortex on 20 July 1990 at 2017 h and $z = 1$ km. The contour intervals, *etc.*, are the same as in figure 2. The rectangles indicate averaging regions discussed later.

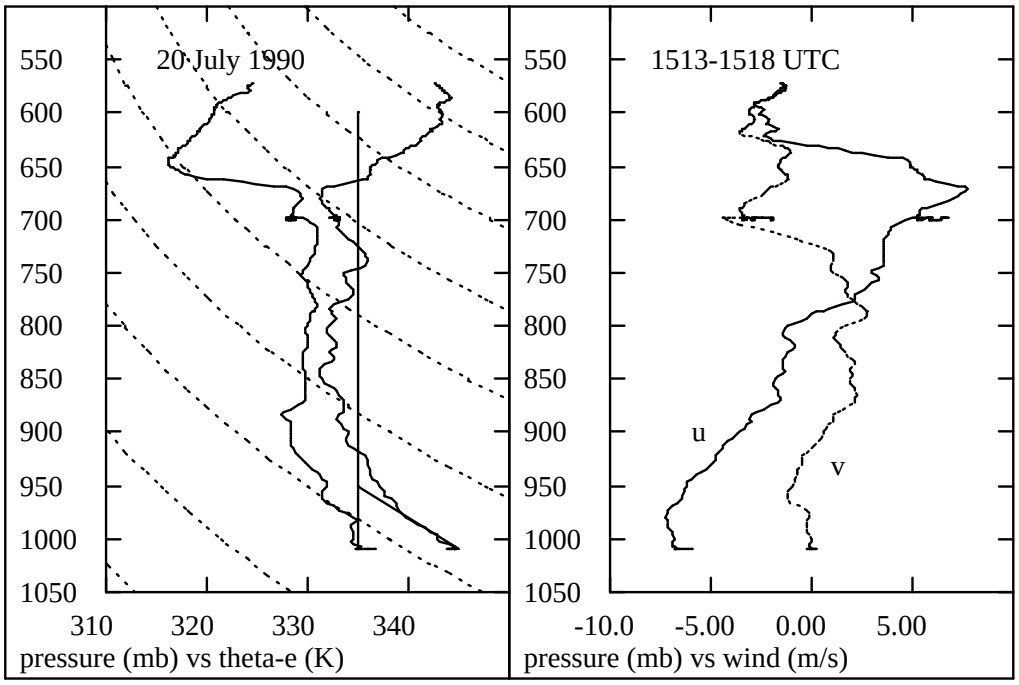

Figure 4: Sounding from the Electra taken in clear air approximately 100 km northeast of the vortex of 20 July 1990. The left panel shows equivalent potential temperature (left curve) and saturated equivalent potential temperature (right curve) plotted against pressure. The vertical and slanted lines illustrate the ascent of a surface parcel. The right panel shows the westerly (u) and southerly (v) components of the wind.

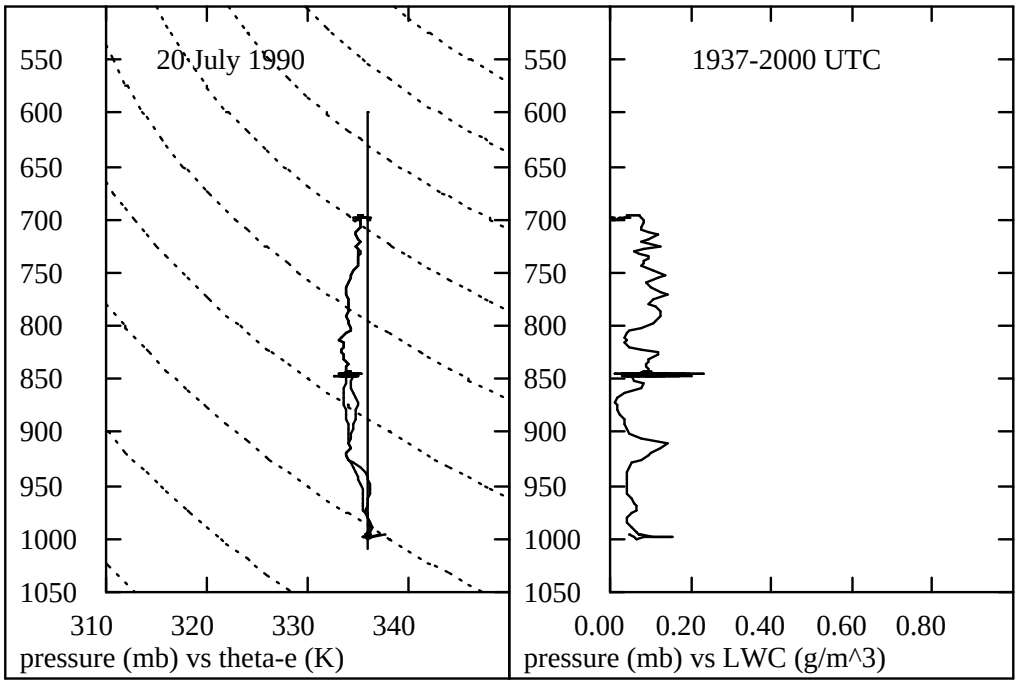

Figure 5: Sounding from the Electra taken through the central region of the vortex. See figure 4 for an explanation of the left panel. The right panel is the liquid water content during the sounding as measured by the FSSP. The sounding was interrupted at 850 mb for a traverse through the system.

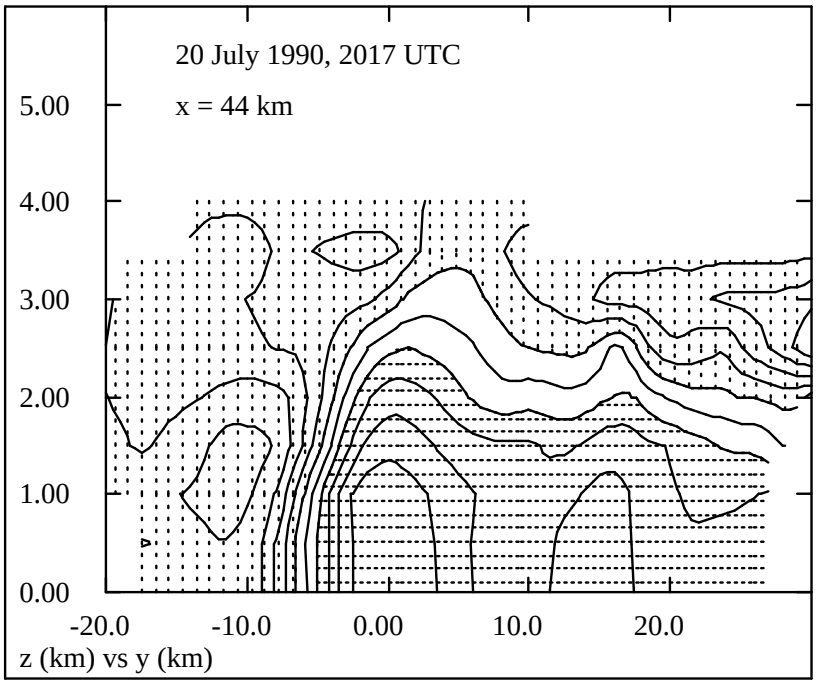

Figure 6: Storm-relative x-component of the wind in a north-south section at $x = 44$ km for 20 July 1990 case. The time is the same as in figure 3. The contour interval on the relative wind is 1 m s^{-1}, with vertical hatching for values exceeding 1 m s^{-1} and horizontal hatching for values less than -1 m s^{-1}.

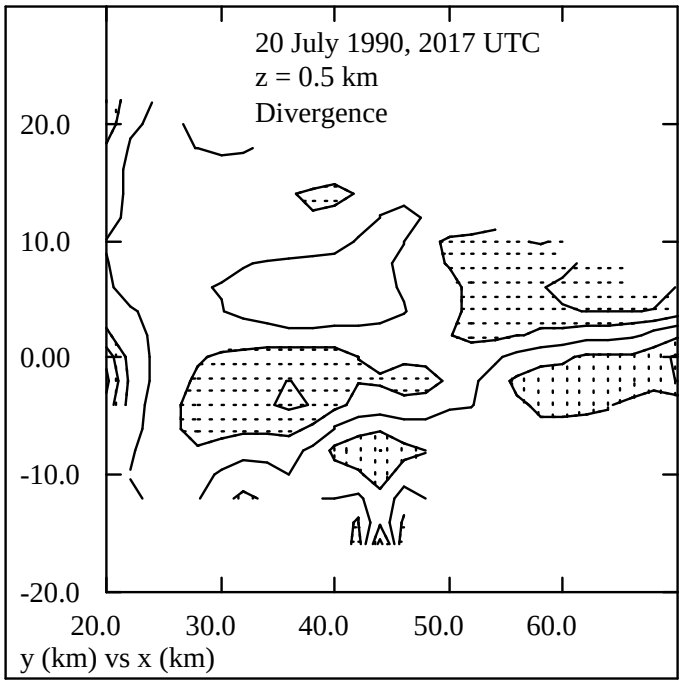

Figure 7: Divergence, $\nabla_h \cdot \boldsymbol{u}$, in horizontal cut at $z = 0.5$ km of 20 July 1990 storm at time of figure 3. The contour interval is 0.25 ks^{-1}. Values greater than 0.25 ks^{-1} have vertical hatching, while values less than -0.25 ks^{-1} have horizontal hatching.

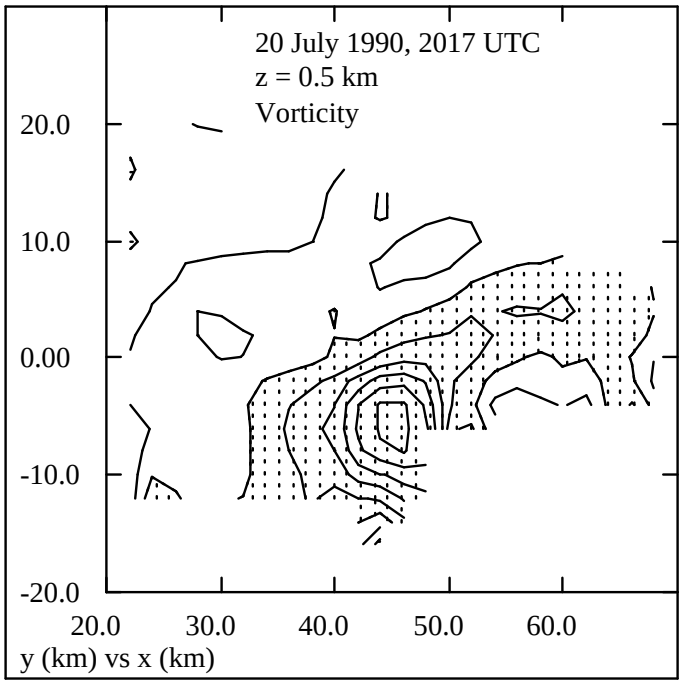

Figure 8: Absolute vorticity, ζ_z, in horizontal cut at $z = 0.5$ km of 20 July 1990 storm at time of figure 3. The contour interval is 0.25 ks^{-1} and values greater than 0.25 ks^{-1} have vertical hatching.

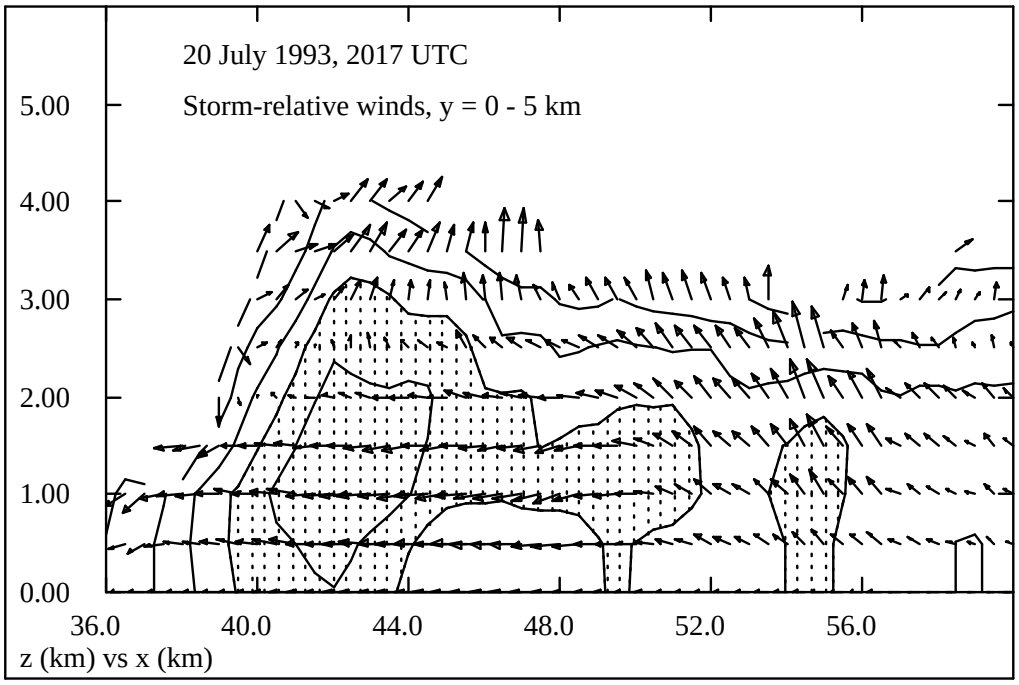

Figure 9: East-west cut averaged over $0 \leq y \leq 5$ km. The cut is along the inflow path to the convection creating the high reflectivity area in figure 3. The reflectivity is contoured at intervals of 5 dBZ, with vertical hatching for reflectivities exceeding 20 dBZ. The velocities are relative to the motion of the vortex, and the velocity scale is 5 m s^{-1} km^{-1}.

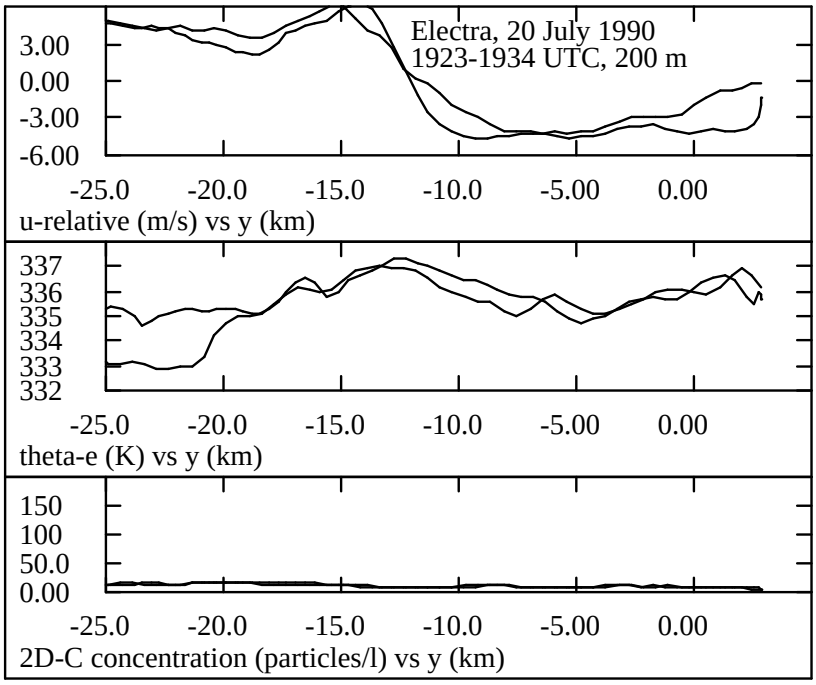

Figure 10: Traverse of the Electra through the vortex of 20 July 1990 from 1923 h to 1934 h at 200 m. The top panel shows the storm-relative westerly wind component, the middle panel the equivalent potential temperature, and the bottom panel the PMS 2D-C particle concentration. Navigational errors locate everything about 5 km south of where it should be when compared to radar observations.

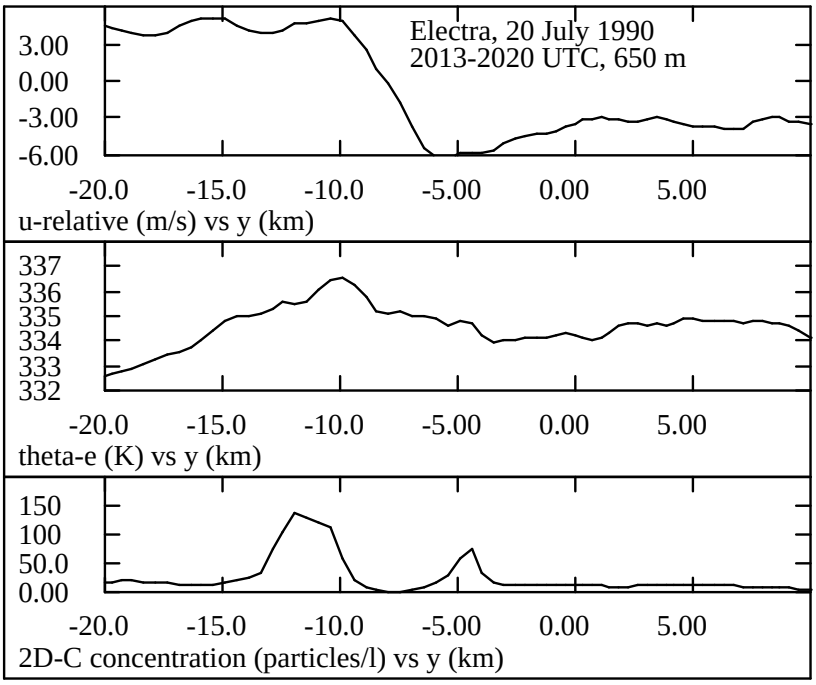

Figure 11: Traverse of the Electra through the vortex of 20 July 1990 from 2013 h to 2020 h at 650 m. The top panel shows the storm-relative westerly wind component, the middle panel the equivalent potential temperature, and the bottom panel the PMS 2D-C particle concentration.

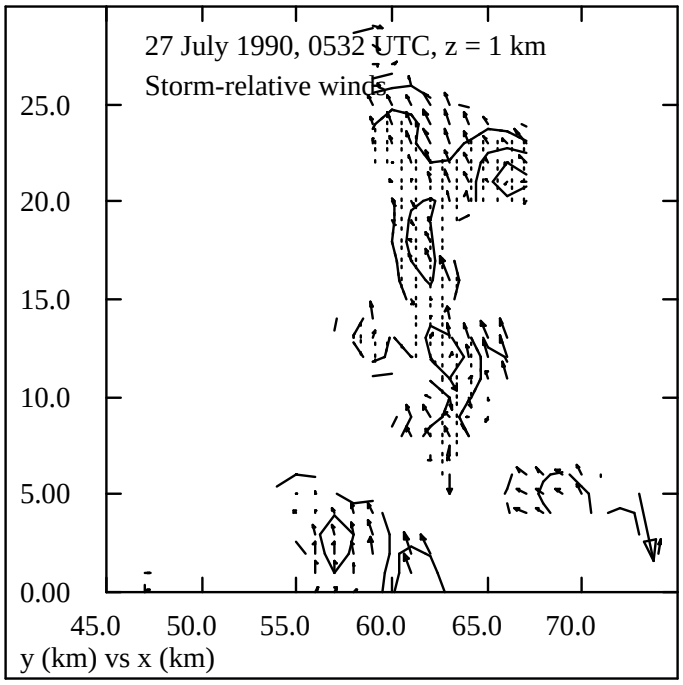

Figure 12: Storm-relative horizontal winds and reflectivity of storm on 27 July 1990 at 0532 h and $z = 1$ km. See figure 3 for contour intervals, *etc.* Data were thinned to a 1 km grid.

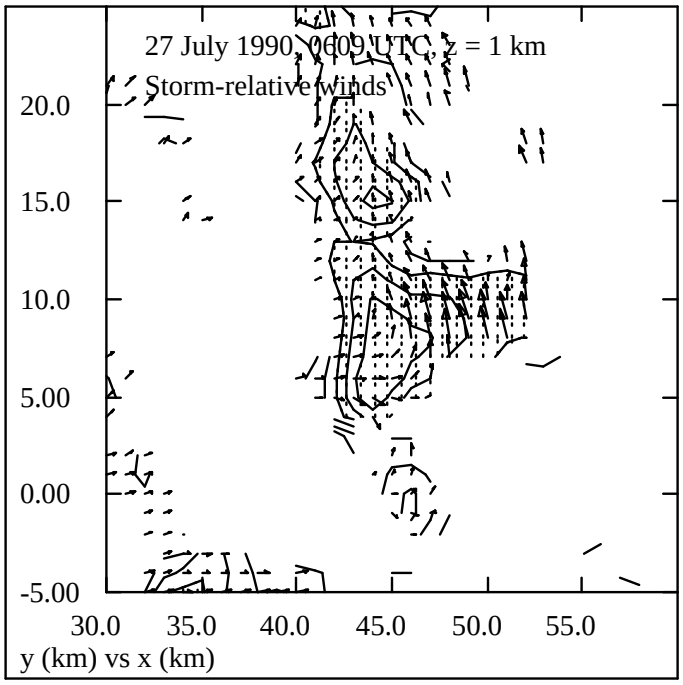

Figure 13: Storm-relative horizontal winds and reflectivity of storm on 27 July 1990 at 0609 h and $z = 1$ km. See figure 3 for contour intervals, *etc.* Data were thinned to a 1 km grid.

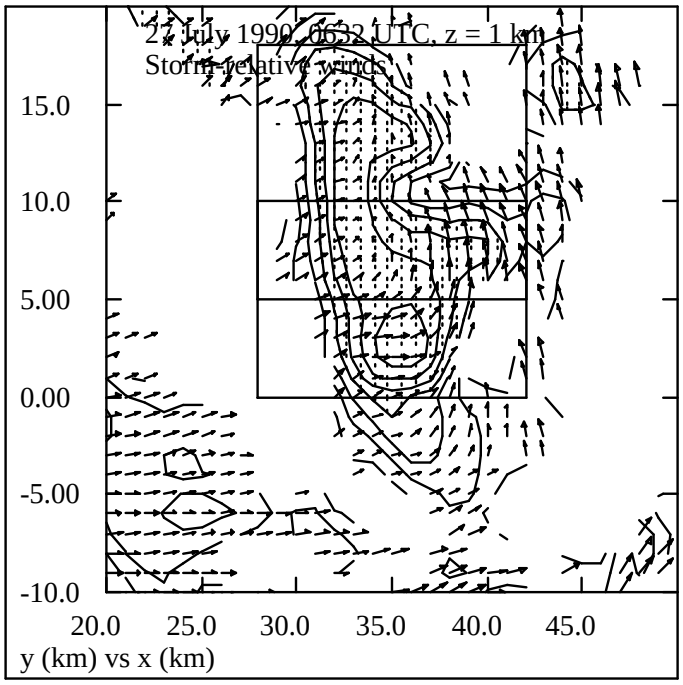

Figure 14: Storm-relative horizontal winds and reflectivity of storm on 27 July 1990 at 0632 h and $z = 1$ km. See figure 3 for contour intervals, *etc.* Data were thinned to a 1 km grid. The rectangles indicate averaging regions discussed later.

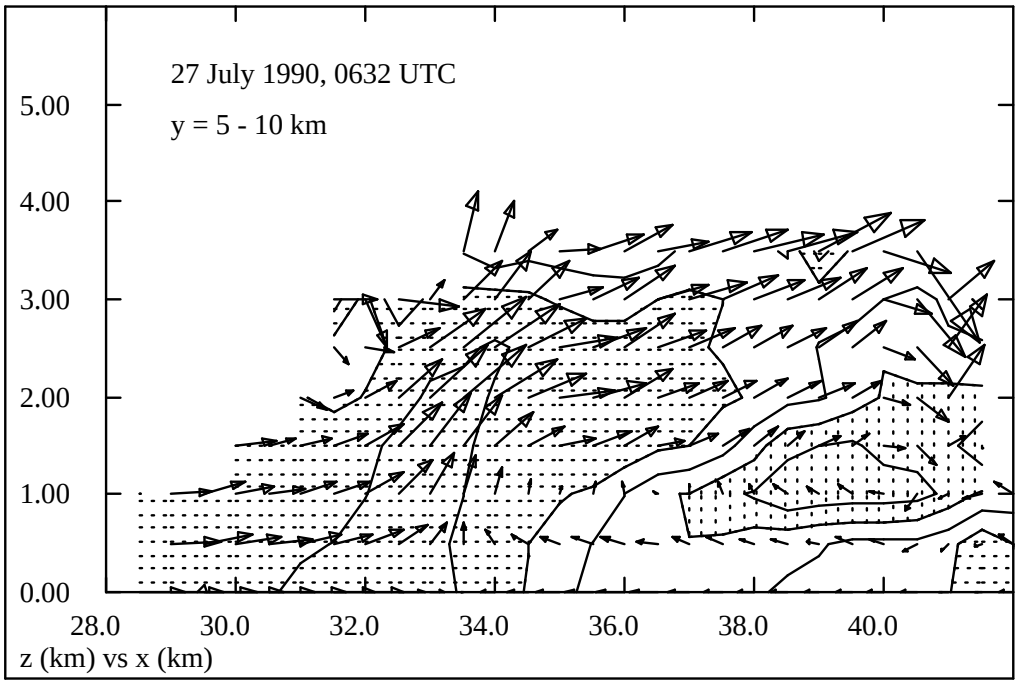

Figure 15: Storm-relative wind components in an east-west section averaged over $5 \leq y \leq 10$ km for 27 July case. The southerly relative wind component is contoured at intervals of 1 m s^{-1}, with horizontal hatching showing winds less than 2 m s^{-1} and vertical hatching showing winds exceeding 4 m s^{-1}. The vectors show winds in the plane of the figure with a scale of 5 m s^{-1} km^{-1}.

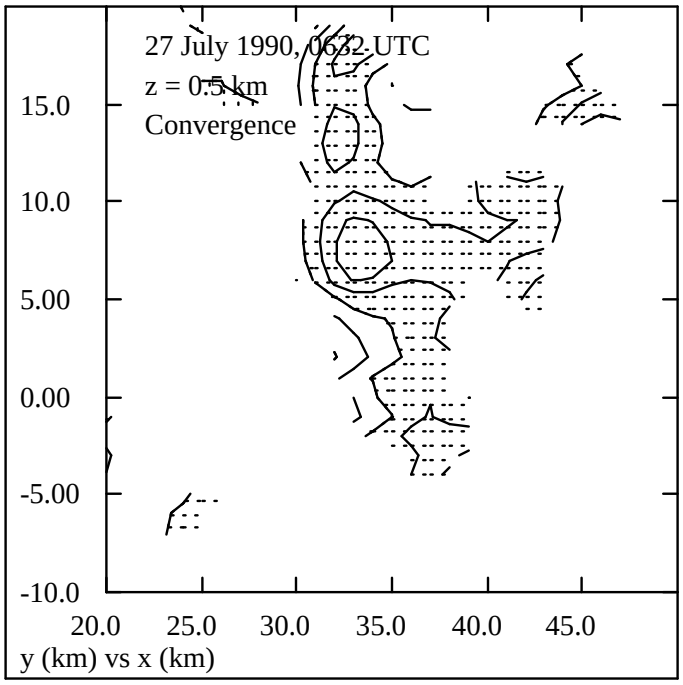

Figure 16: Divergence in horizontal cut at $z = 0.5$ km of 27 July 1990 storm at 0632 h. See figure 7 for contour information.

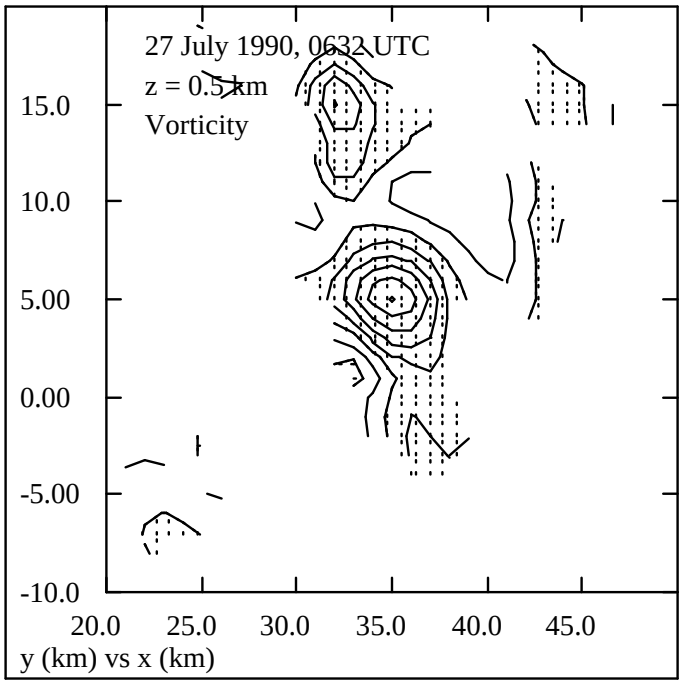

Figure 17: Absolute vorticity in horizontal cut at $z = 0.5$ km of 27 July 1990 storm at 0632 h. See figure 8 for contour information.

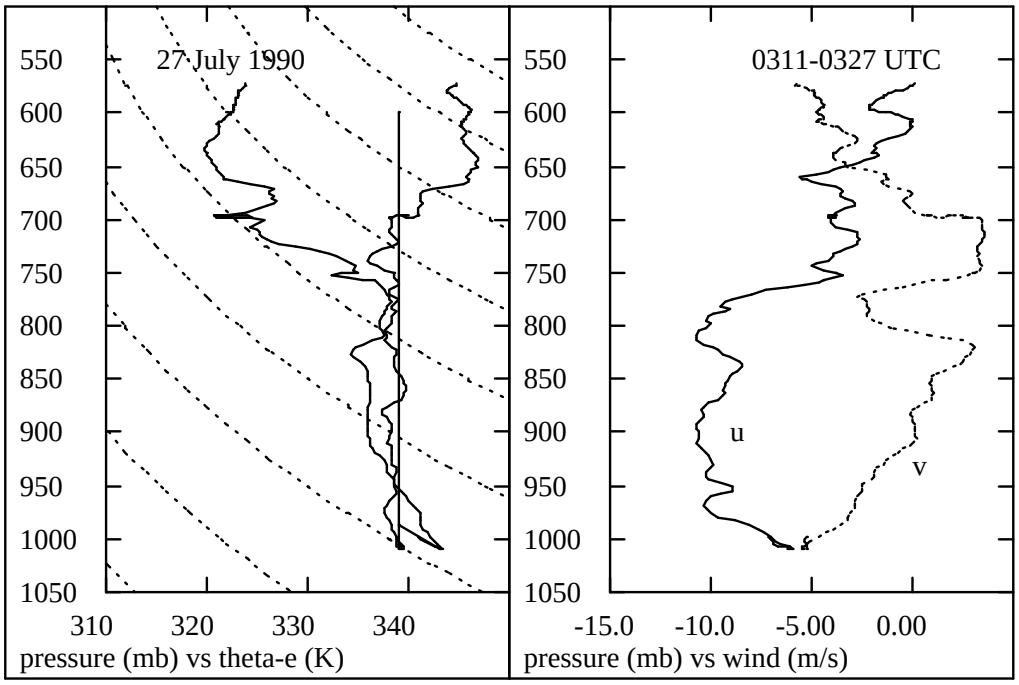

Figure 18: Sounding from the Electra taken across the shear line on 27 July 1990. See figure 4 for details.

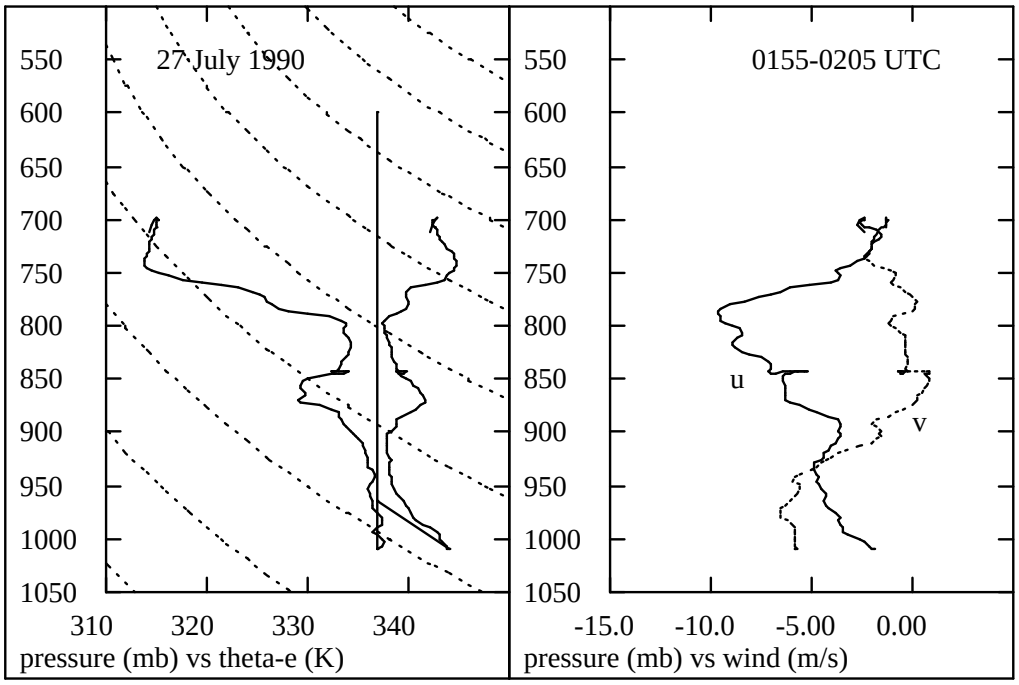

Figure 19: Sounding from the Electra taken 150 km southwest of the studied storm on 27 July 1990. See figure 4 for details.

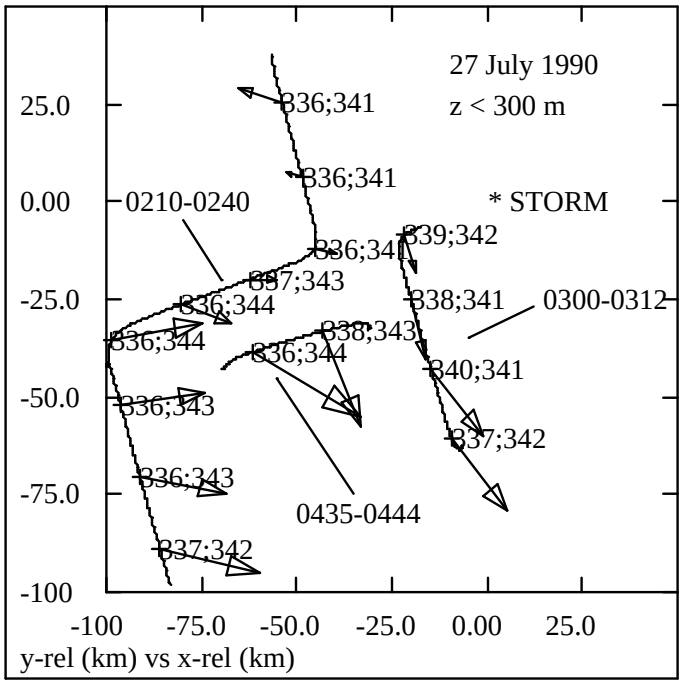

Figure 20: Series of Electra traverses below 300 m elevation to west of shear line. The $x - y$ coordinate system moves with the studied storm, which is located at the origin. The numbers show θ_e and θ_{es} at each point, and the wind vector scale is 5 m s^{-1} per 25 km.

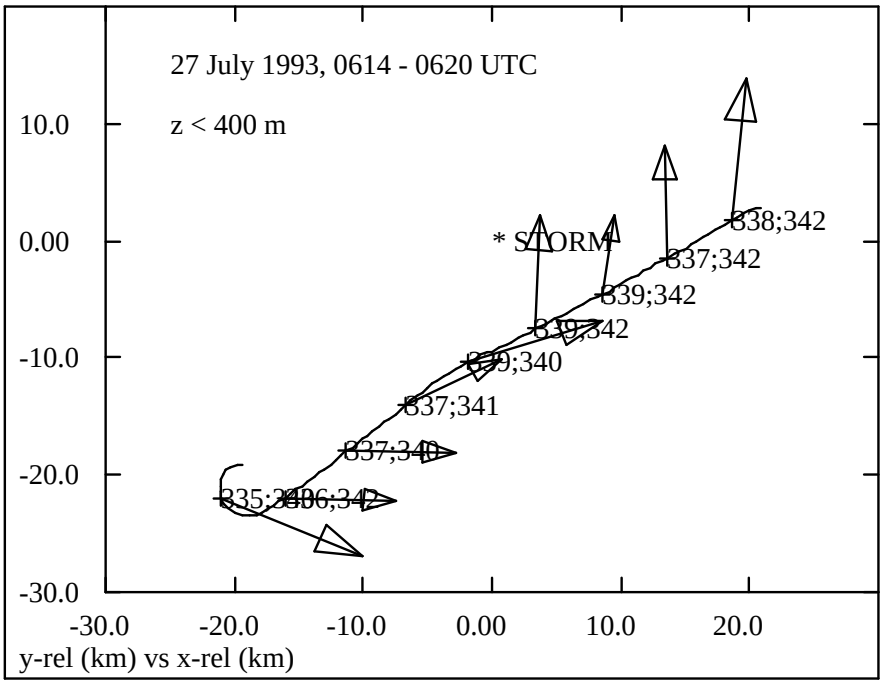

Figure 21: Electra traverse through the shear line. Elevation was near $z = 300$ m. The $x - y$ coordinate system moves with the studied storm, which is located at the origin. The numbers show θ_e and θ_{es} at each point, and the wind vector scale is 5 m s^{-1} per 10 km.

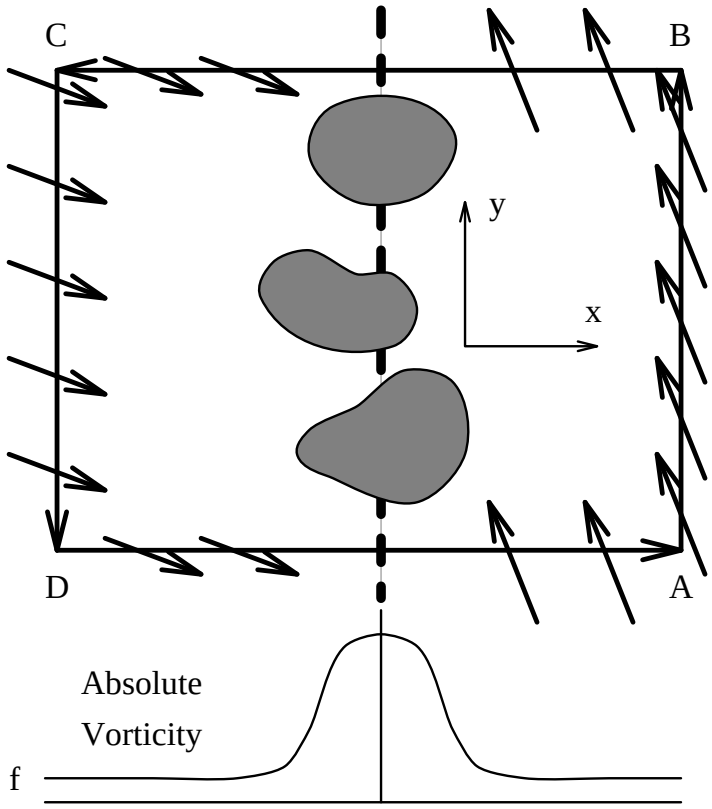

Figure 22: Schematic illustration of 27 July case and a region ABCD for integrating (7). The shaded areas are convective cells along the shear line, denoted by the heavy dashed line. The plot at the bottom shows how absolute vorticity might vary across the line, from f away from the line to many times f at the line.

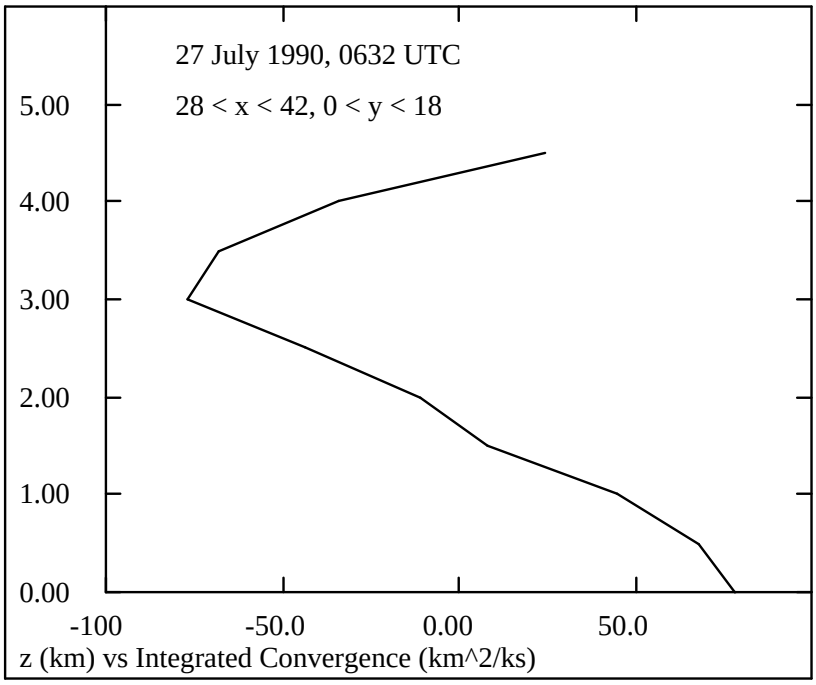

Figure 23: Vertical profile of integrated convergence, K, for the 27 July case at 0632 h. The areal integration was confined to the limits indicated in the figure. These limits are illustrated by the large rectangle in figure 14.

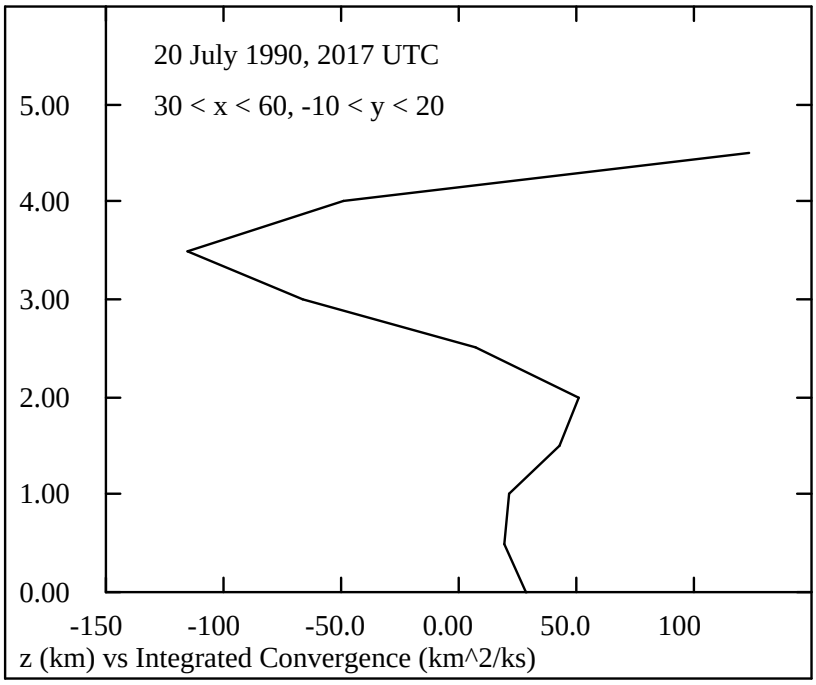

Figure 24: Vertical profile of integrated convergence, K, for the 20 July case at 2017 h. The areal integration was confined to the limits indicated in the figure. These limits are illustrated by the large rectangle in figure 3.

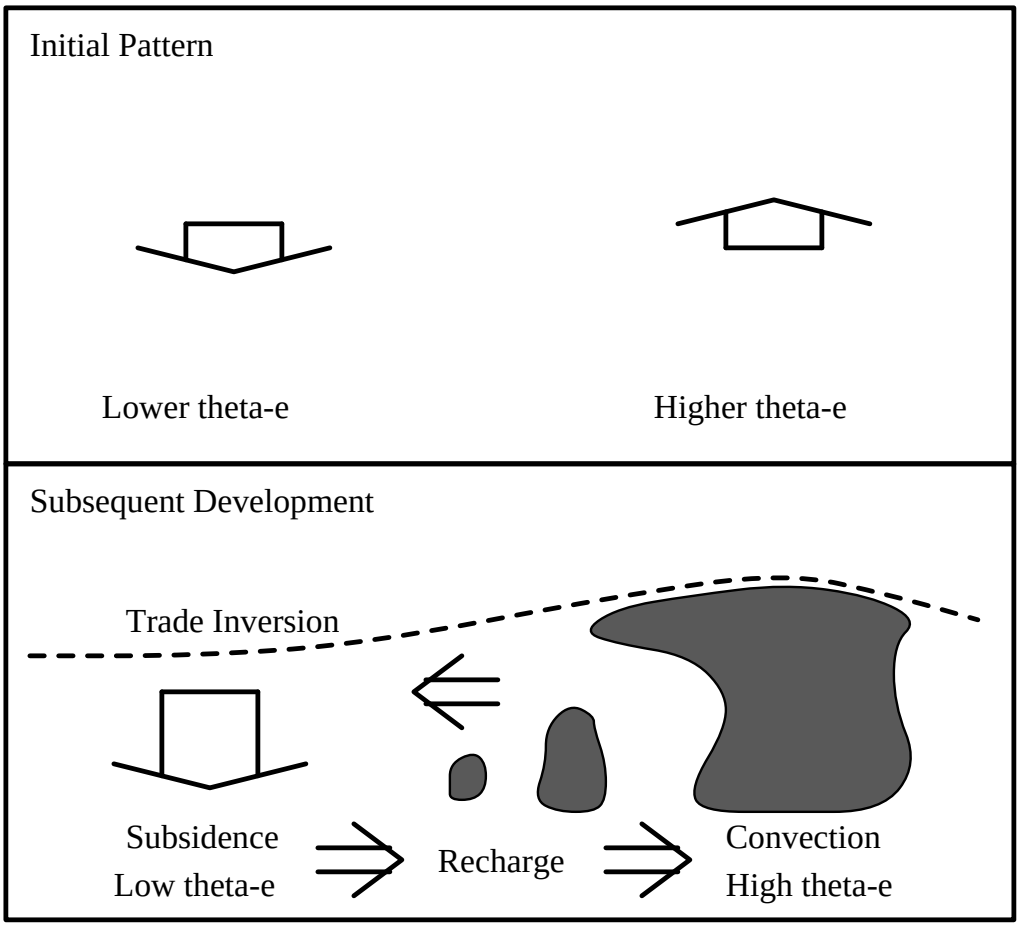

Figure 25: Illustration of the development of a mesoscale circulation driven by a gradient in the boundary layer equivalent potential temperature. Parcels rising from the boundary layer are more buoyant where θ_e is higher, resulting in mean ascent. This in turn reduces entrainment from above, allowing surface fluxes to further increase boundary layer θ_e. The opposite effect occurs in subsidence regions, where mixing of low θ_e air down from aloft decreases boundary layer θ_e. Boundary layer equivalent potential temperature increases as air moves through the recharge region where subsidence is weak.